AIChE

CFD Modeling of the Wurster Bed Coater

Stina Karlsson and Anders Rasmuson
Dept. of Chemical and Biological Engineering, Chalmers University of Technology, SE-412 96 Gothenburg, Sweden

Berend van Wachem
Dept. of Applied Mechanics, Chalmers University of Technology, SE-412 96 Gothenburg, Sweden

Ingela Niklasson Björn
AstraZeneca Pharmaceutical and Analytical R&D, Mölndal, SE-431 83 Mölndal, Sweden

DOI 10.1002/aic.11847
Published online August 26, 2009 in Wiley InterScience (www.interscience.wiley.com).

In the Wurster bed coater, the wetting, drying, and circulation of particles are combined to produce a high quality coating. The drying and wetting conditions in a laboratory scale Wurster bed coater are modeled and compared with experimental data. A model combining multiphase fluid dynamics with heat and mass transfer is developed to model the particle and gas motion and the transport of thermal energy and moisture. A wetting region is defined, where a specified moisture content is set in the particle phase, above the jet inlet, to describe the injection of coating liquid. The simulation shows the characteristic circulation of particles in the equipment, as well as the behavior of the moisture in the system and agrees well with measurements. The simulation indicates how different process conditions influence the drying regions. The results show that most of the drying, under typical operating conditions, takes place in the Wurster tube. © 2009 American Institute of Chemical Engineers *AIChE J,* 55: 2578–2590, 2009

Keywords: coating, fluidized bed, drying, CFD, Wurster

Introduction

The Wurster process is a common technique used in the pharmaceutical industry to coat tablets and smaller particles in the range of 20–1000 μm. The Wurster bed is a type of spouted bed with a draft tube and fluidisation flow around the jet, Figure 1. The jet consists of a spray nozzle injecting air and droplets of coating liquid into the bed. The droplets hit the particles concurrently in the inlet to the draft tube. The particles are transported upwards through the tube, decelerate in the expansion chamber and fall down to the dense region of particles outside the tube. During the upward movement and the deceleration, the particles are dried by the warm air. From the dense region the particles are transported again into the Wurster tube where the droplets hit the particles, and the circulation motion in the bed is repeated. The particles are circulated until a thick enough layer of coating material has been built up around them.

The Wurster process is controlled by many parameters, which can influence the quality of the coating layer. Although operating conditions and the equipment geometry have been developed through experiments and experience of the process, the actual influence of the fundamental mechanisms in the process is not well understood. The drying rate, and hence the film formation, is highly dependent on the flow field of the gas and the particles in the equipment. Local temperatures in the equipment are also critical for the film formation; different temperatures may change the properties of the coating layer. The temperature is also

Correspondence concerning this article should be addressed to A. Rasmuson at rasmuson@chalmers.se

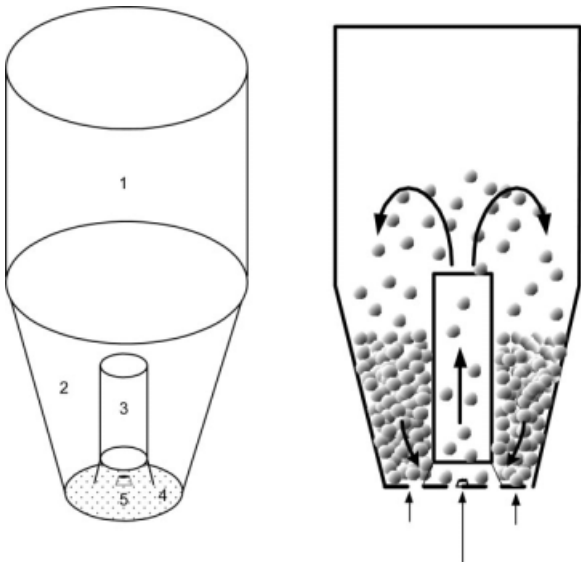

Figure 1. Schematic drawings of a Wurster bed.

1, Expansion chamber (deceleration region, fountain); 2, annulus (down bed region); 3, Wurster tube (up bed region); 4, distributor plate; 5, spray nozzle.

important for the moisture equilibrium and influences the drying rate. Maronga and Wnukowski[1] showed that distinct temperature regions can be identified in a top spray fluidized bed; the temperature level gives an indication that the process works correctly. In the manufacturing scale equipment, the moisture content of the air varies with the seasons, which can influence the coating quality. A typical air quality for the manufacturing scale is 35% RH at 20°C. Hence, a model of the Wurster process should include predictions of both the temperature and the moisture content in the coating layer, as well as in the air at different positions in the bed.

The coating liquid used in this study is water-based latex dispersion. Drying and film formation of latex dispersions is often divided into three stages. Vanderhoff et al.[2] describe the three stages: evaporation of water brings the latex particles into irreversible contact; latex particles deform to form a film without voids; and polymer chains diffuse across the latex particles interfaces to form a continuous film.

At the first stage, water evaporates from the surface and the film dries at a constant rate. The drying rate depends on the temperature and the relative humidity of the air, as well as the flow conditions. The dimensionless external mass transfer coefficient, Sh_p, is a function of the Reynolds, Re, and the Schmidt, Sc, numbers. Correlations for Sh_p may be found in the literature. How well the latex particles pack before the second stage starts, deformation of particles, depends on both the properties of the latex particles and the drying rate. The deformation starts somewhere in the dry content range $0.52 < dc < 0.74$, where $dc = 0.52$ corresponds to simple cubic packing, and $dc = 0.74$ corresponds to an ideal face centred cubic (fcc) close packed bed. The rate of drying decreases during this second stage. In stage 3, particles coalesce and a continuous film is formed. The drying rate decreases further, and the remaining water diffuses through the polymer itself.

Christensen and Bertelsen[3] divided the Wurster process into five regions according to the particle movement. These regions are illustrated in Figure 1. Modeling of the Wurster process is often based on dividing the process into regions. Each region is typically modeled separately. Sherony[4] was one of the first to model the coating process by dividing the equipment into a spraying and a drying region. Maronga and Wnukowski[5] used three regions to model the particle movement in top spray coating equipment. Turton[6] presents a review of several types of models used to describe the coating process used for pharmaceutical applications.

Magnusson et al.[7] used multiphase computational fluid dynamics (CFD) to develop a 3D model of the particle and gas motion in the Wurster process. The simulation results, which are compared with measurements of the solid volume fraction, give good prediction of both dense and dilute regions in the equipment. Making an accurate description of the particle and gas dynamics in the 3D model is time consuming; if the wetting and drying are to be included in the model, the computation time will be increased further. Szafran and Kmiec[8] combined an axi-symmetric CFD simulation of the particle and gas motion of a spouted bed dryer, including models for heat and mass transfer. The spouted bed dryer is a batch process, by which wet particles are loaded and circulate in the bed until they are dry. The Wurster process, on the other hand, is a semicontinuous process by which the particles are loaded in the equipment and the liquid is sprayed continuously into the bed.

The aim of this study is to develop a model of the Wurster process by combining the gas and particle dynamics with mass and heat transfer. The particle and gas motion are predicted by using multiphase CFD, which provides detailed information about the flow field, temperature, and moisture content.

The model is validated with experimental and theoretical work carried out in our group. The results of the model are used to analyze the local drying properties of the equipment and the effect of geometric properties and operating conditions on the drying process. Moreover, information on the temperature profiles in the bed is provided, which can be important, for example, to determine the maximum and minimum temperatures the particles are subjected to during the entire process. In addition to optimizing operating conditions and geometric properties of the equipment, this model also increases the understanding of the hydrodynamics of the bed and its effect on the drying process.

Mathematical models

Model for the particle and gas movement

In the laboratory scale Wurster bed studied in this work, approximately 2×10^6 particles are coated in one batch. To enable the simulation of such a system in a reasonable length of time, the Eulerian-Eulerian, or two fluid model, is used to simulate the particle and gas motion in the bed. In

Table 1. Governing Equations for Particle and Gas Movement

Continuity equations for particle and gas phase (g = gas, p = particle)

$$\frac{\partial}{\partial t}(\alpha_p \rho_p) + \nabla \cdot (\alpha_p \rho_p \mathbf{u}_p) = 0$$
$$\frac{\partial}{\partial t}(\alpha_g \rho_g) + \nabla \cdot (\alpha_g \rho_g \mathbf{u}_g) = 0 \quad (21)$$

Momentum equations for particle and gas phase[9]

$$\frac{\partial}{\partial t}(\alpha_p \rho_p \mathbf{u}_p) + \nabla \cdot (\alpha_p \rho_p \mathbf{u}_p \mathbf{u}_p) = -\alpha_p \nabla p - \nabla p_p + \nabla \cdot \alpha_p \overline{\tau_p} + \alpha_p \rho_p \mathbf{g} + \beta(\mathbf{u}_g - \mathbf{u}_p)$$
$$\frac{\partial}{\partial t}(\alpha_g \rho_g \mathbf{u}_g) + \nabla \cdot (\alpha_g \rho_g \mathbf{u}_g \mathbf{u}_g) = -\alpha_g \nabla p + \nabla \cdot \alpha_g \overline{\tau_g} + \alpha_g \rho_g \mathbf{g} - \beta(\mathbf{u}_g - \mathbf{u}_p) \quad (22)$$

Gas phase stress

$$\overline{\tau_g} = \mu_g\left(\nabla \mathbf{u}_g + (\nabla \mathbf{u}_g)^T\right) + \left(\lambda_g - \frac{2}{3}\mu_g\right)\nabla \cdot \mathbf{u}_g \bar{\mathbf{I}} \quad (23)$$

Solid phase stress

$$\overline{\tau_p} = \mu_p(\nabla \mathbf{u}_p + (\nabla \mathbf{u}_p)^T) + \left(\lambda_p - \frac{2}{3}\mu_p\right)\nabla \cdot \mathbf{u}_p \bar{\mathbf{I}} \quad (24)$$

the Eulerian-Eulerian model, both gas and the particles are modeled as continuous, interpenetrating phases and the continuity and the momentum equations are solved for each phase, Table 1.[9] The explanation of the symbols in the tables can be found in the notation. Because the averaged nature of the Eulerian-Eulerian model, closure relations are required. The closure models used in this work are described in the next section.

Closures

The application of kinetic theory of granular flow (KTGF) has become a generally accepted concept to provide closures for the particle phase momentum equations. The original KTGF model accounts for the particulate stresses of low and moderate particle volume fractions. It has been shown that this model, in conjunction with a frictional stress model, works well for moderate to dense gas-particle flows, such as fluidized bed modeling.[10]

Equivalent to the thermodynamic temperature for gases, the granular temperature can be introduced as a measure for the energy of the fluctuating velocity of the particles. The granular temperature, Θ_p is defined as

$$\Theta_p = \frac{1}{3}\mathbf{u}_p'^2 \quad (1)$$

where $\mathbf{u}'_p$ is the fluctuating velocity of the particles. The equation of conservation of the fluctuating energy of the particles can be found in Ding and Gidaspow[11]:

$$\frac{3}{2}\left[\frac{\partial}{\partial t}(\alpha_p \rho_p \Theta_p) + \nabla \cdot (\alpha_p \rho_p \mathbf{u}_p \Theta_p)\right] = (-p_p \bar{\mathbf{I}} + \overline{\tau_p}) : \nabla \mathbf{u}_p - \nabla \cdot (\kappa_p \nabla \Theta_p) - \gamma_p - J_p \quad (2)$$

where κ_p is the diffusion coefficient, γ_p is the dissipation of fluctuating energy, and J_p is the exchange of fluctuating energy between the phases. The closures are given in Table 2, where g_0 is the radial distribution function, e_{pp} is the coefficient of restitution of colliding particles, as a measure for the nonidealness of the particle-collision, and d_p is the particle diameter. The radial distribution function corrects for

Table 2. Closure Relations Provided by the Kinetic Theory of Granular Flow

Radial distribution function[13]

$$g_0 = \left[1 - \left(\frac{\alpha_p}{\alpha_{p,max}}\right)^{\frac{1}{3}}\right]^{-1} \quad (25)$$

Particle pressure[13]

$$p_p = \alpha_p \rho_p \Theta_p + 2\rho_p(1 + e_{pp})\alpha_p^2 g_0 \Theta_p \quad (26)$$

Collisional dissipation of energy[13]

$$\gamma_p = \frac{12(1 - e_{pp}^2)g_0}{d_p\sqrt{\pi}}\rho_p \alpha_p^2 \Theta_p^{3/2} \quad (27)$$

Particle bulk viscosity[13]

$$\lambda_p = \frac{4}{3}\alpha_p \rho_p d_p g_{0,pp}(1 + e_{pp})\left(\frac{\Theta_p}{\pi}\right)^{1/2} \quad (28)$$

Particle shear viscosity

$$\mu_p = \mu_{p,kin} + \mu_{p,fr} \quad (29)$$

Kinetic particle shear viscosity[14]

$$\mu_{p,kin} = \frac{10\rho_p d_p \sqrt{\Theta_p \pi}\left[1 + \frac{4}{5}g_{0,pp}\alpha_p(1 + e_{pp})\right]^2}{96\alpha_p(1 + e_{pp})g_{0,pp}} + \frac{4}{5}\alpha_p \rho_p d_p g_{0,pp}(1 + e_{pp})\left(\frac{\Theta_p}{\pi}\right)^{1/2} \quad (30)$$

Normal frictional stress[16]

$$P_{fr} = Fr\frac{(\alpha_p - \alpha_{p,min})^{nn}}{(\alpha_{p,max} - \alpha_p)^{pp}} \quad (31)$$

Frictional shear viscosity[17]

$$\mu_{p,fr} = \frac{P_{fr}\sin(\phi)}{\alpha_p\sqrt{I_{2D}}} \quad (32)$$

the chaos assumption which fails at higher particle volume fractions and is typically given by Eq. 25 in Table 2.

The particle pressure, p_p, represents the particle phase normal forces due to particle–particle interactions. Its description, based on the kinetic theory of granular flow, was developed by Jenkins and Savage[12] and Lun et al.[13] In this approach, both the kinetic and the collision influences are taken into account. The kinetic part describes the influence of particle translations, whereas the collision term accounts for the momentum transfer by direct collisions. The particle pressure is given by Eq. 26 in Table 2.

The bulk viscosity is a measure for the resistance of a fluid against compression. It is obvious that the importance of the bulk viscosity depends strongly on the velocity gradients. In a fluidized bed, the bulk viscosity and the shear viscosity are of the same order of magnitude, and hence the bulk viscosity should not be neglected, as is done in simulating Newtonian fluids. The bulk viscosity as predicted by KTGF is given by Eq. 28 in Table 2.

Although pressure and bulk viscosity describe normal forces, the shear viscosity accounts for the tangential forces. It was shown by Lun et al.[13] that it is possible to combine different interparticle forces and to use a momentum balance similar to that of a true continuous fluid. In similarity to the particle pressure, a particle shear viscosity can be derived from the kinetic theory. The shear viscosity comprises two terms: one for the dilute region and another for the dense region. In the literature different expressions for the solids shear viscosity can be found. The work of Gidaspow et al.[14] is validated by comparison with measured data and given by Eq. 30 in Table 2.

To reduce computational effort, the assumption is made that the granular energy produced locally is dissipated locally, as the advection and diffusion of granular energy are of minor importance. Then, only the generation and dissipation terms are retained from Eq. 2:

$$0 = \left(-p_p\bar{\bar{I}} + \overline{\tau_p}\right) : \nabla \mathbf{u}_p - \gamma_p \tag{3}$$

This leads to an algebraic equation for the granular energy. The procedure has been proven correct for simulations of dense flows.[10]

At high solid volume fraction, sustained contacts between particles occur and the stresses predicted by kinetic theory of granular flow are insufficient. Hence, the additional frictional stresses must be accounted for in the description of the particle phase stress. Zhang and Rauenzahn[15] conclude that particle collisions are no longer instantaneous at high solid volume fractions, as is assumed in kinetic theory. Several approaches have been presented in the literature to model the frictional stress, mostly originating from geological research groups. Usually, the frictional stress is written in a Newtonian form and has both a deviatoric stress-like contribution and a normal stress-like contribution. The frictional stress is added to the stress predicted by kinetic theory for $\alpha_p > \alpha_{p,\,min}$, where the subscript "min" stands for threshold value. Johnson and Jackson[16] propose a semiempirical equation for the normal frictional stress, Eq. 31 in Table 2, in which Fr, nn, and pp are empirical material constants; $\alpha_{p,\,min}$ is the particle volume fraction when frictional stresses become important. The frictional shear viscosity is then related to the frictional normal stress by the linear law proposed by Schaeffer,[17] Eq. 32 in Table 2.

When modeling the momentum transfer between the gas and the particles, the form and skin drag on the particles are combined in one force, the interphase drag force. This drag force is typically obtained from pressure drop measurements in fixed, fluidized, and settling beds. Although there are many drag force models, described in the literature, the most applicable one is given by Wen and Yu.[18] The drag force is given by

$$\beta = \frac{3}{4} C_D \frac{(1-\alpha_p)\alpha_p \rho_g \left|\mathbf{u}_g - \mathbf{u}_p\right|}{d_p} \left(1-\alpha_p\right)^{-2.65} \tag{4}$$

where ρ_g is the fluid density, $\mathbf{u}_g$ and $\mathbf{u}_p$ are the gas and particle velocities, and α_p is the volume fraction of the particulate phase. The drag coefficient C_D is given by

$$C_D = \begin{cases} \frac{24}{Re_p(1-\alpha_p)}\left[1 + 0.15((1-\alpha_p)Re_p)^{0.687}\right] & \text{if } (1-\alpha_p)Re_p < 1000 \\ 0.44 & \text{if } (1-\alpha_p)Re_p \geq 1000 \end{cases} \tag{5}$$

and the particle Reynolds number is defined as

$$Re_p = \frac{d_p \rho_g \left|\mathbf{u}_g - \mathbf{u}_p\right|}{\mu_g} \tag{6}$$

where d_p represents the mean diameter of particles. This form of the drag force model represents the hydrodynamic forces on the particles. It is noted by Wen and Yu[18] that this model is valid to predict the drag force on fine particles as well.

As a first approximation, the gas phase is assumed to be laminar. As the hydro and thermodynamics of the system are dominated by dense solid flow, this is not expected to be of importance.[10]

Heat and mass transfer

When the particles pass the region close to the spray nozzle, the droplets are deposited and spread out on the particle surface. The amount of liquid deposition on each particle depends on how closely the particle passes the nozzle, the local volume fraction of particles, and the particle velocity in the region close to the nozzle. In this study, the particles are treated as a continuum and a local average moisture content of the particles is assumed as they pass the wetting region. This moisture content fed to the particles is based on the experimental conditions. The penetration depth of the droplets in a jet into a particle bed is taken from the work by Löffler et al.[19] and Heinrich et al.[20] Their study showed that the penetration depth depends on the spray angle, θ_{nozz}, particle volume fraction, particle diameter, and collection efficiency of droplets, φ_{dep}. Heinrich et al.[20] derive an equation for how the deposition of droplets varies with distance from the nozzle outlet, r_n,

$$s = \frac{\dot{m}_L}{2\pi(1-\cos(\theta_{nozz}/2))} \frac{e^{\left(\frac{-r_n}{dz}\right)}}{r_n^2 dz} \tag{7}$$

$$dz = \frac{2}{3}\frac{d_p \alpha_g}{(1-\alpha_g)\varphi_{dep}} \quad (8)$$

where m_i is the spray rate, and dz the average droplet path length.

The moisture content is modeled as a scalar in the particle and gas phases. Simulations of the drying process with scalars representing the moisture has been described by Szafran and Kmiec[8] and Hidayat and Rasmuson.[21] Two transport equations are solved for the moisture content:

$$\frac{\partial \alpha_i \rho_i w_i}{\partial t} + \nabla \cdot (\alpha_i \rho_i \mathbf{u}_i w_i) = \nabla \cdot (\alpha_i \Gamma_i \nabla w_i) + S_{w,i} \quad (9)$$

where subscript i is gas or particle phase, and w is the mass fraction of water.

The drying model is based on the work of Vanderhoff et al.[2] that describes the film formation of latex dispersions and divides the formation into three stages. Studies in the literature show that the initial evaporation rate of latex dispersions is the same as for pure water.[2,22] To model the first drying region, the air close to the particle surface is assumed to be saturated with water:

$$N^I_{w,p} = \frac{k_{pg} M_w}{R}\left(\frac{p_{w,sat}}{T_p} - \frac{p_{w,g}}{T_g}\right) \quad \text{if } dc \le dc_c = 0.40 \quad (10)$$

The drying rate is controlled by convection, and the correlation given by Gunn[23] is used to calculate the mass transfer coefficient, k_{pg}, between the phases:

$$\begin{aligned} Sh_p &= (7 - 10\alpha_g + 5\alpha_g^2)(1 + 0.7Re_p^{0.2}Sc^{1/3}) \\ &\quad + (1.33 - 2.4\alpha_g + 1.2\alpha_g^2)\mathrm{Re}_p^{0.7}Sc^{1/3} \\ k_{pg} &= \frac{D_{AB} Sh_p}{d_p} \end{aligned} \quad (11)$$

where D_{AB} is the diffusivity of water in air.

The drying that occurs in stages 2 and 3 is disregarded in the simulation. As a first approximation, the drying rate is assumed to decrease according to Eq. 12 when the dry content (dc), in the coating layer is 0.4; the drying rate is set to zero when a dry content of 0.64, random close packed bed, is reached.

$$N^{II}_{w,p} = \frac{dc - dc_e}{dc_c - dc_e} N^I_{w,p} \quad \text{if } 0.40 < dc \le 0.64 \quad (12)$$

$$N^{III}_{w,p} = 0 \quad \text{if } dc > dc_e = 0.64 \quad (13)$$

The mass transfer between the phases is described by the source terms, Eq. 14, in the transport equations of the scalars.

$$\begin{aligned} S_{w,p} &= -\frac{6\alpha_p N_{w,p}}{d_p} \\ S_{w,g} &= -S_{w,p} \end{aligned} \quad (14)$$

Because the energy content is central for the drying, it is necessary to include the energy equation in the model:

$$\frac{\partial}{\partial t}(\alpha_i \rho_i H_i) + \nabla \cdot (\alpha_i \rho_i \mathbf{u}_i H_i) = -\alpha_i \frac{\partial p_i}{\partial t} + \overline{\overline{\tau_i}} : \nabla \mathbf{u}_i + Q_{ji} + S_{h,i} \quad (15)$$

where Q_{ji} is the heat exchange between gas and particle phases, and $S_{h,i}$ is the energy transfer due to evaporation. The heat is exchanged between the phases by convection:

$$Q_{pg} = \frac{6\alpha_p \alpha_g h_{pg}(T_p - T_g)}{d_p} \quad (16)$$

where h_{pg} is the heat transfer coefficient. The correlation given by Gunn[23] for heat transfer was used to estimate the heat transfer coefficient. The equation is obtained by substituting Nu for Sh and Pr for Sc in Eq. 11.

To account for the energy required to evaporate moisture, a source term is added to the energy equation in the particle phase:

$$S_{h,p} = S_{w,p} H_{vap,w} \quad (17)$$

where $H_{vap,w}$ is the energy for evaporation of water obtained by[21]:

$$H_{vap,w} = 3006300 - 1428.1T_p - 1.5534T_p^2 \quad (18)$$

A particle circulating in the equipment has a varying relative velocity to the gas, and it passes through regions of differing gas temperatures and humidities, which is why the drying rate varies along the particle trajectory in the bed; with the CFD model, this variation is accounted for in detail.

Experimental set-up

The operating conditions for the numerical cases are summarized in Table 3. The base case is specified in accordance with experimental operating conditions for the laboratory scale bed. Test cases 1–3 are chosen to investigate the influence of temperature, spray rate, and air humidity on the coating process. A schematic drawing of the laboratory scale Wurster bed is given in Figure 1, and the geometric dimensions in Table 4 and Figure 2. The properties of the

Table 3. Operating variables

Variable	Base Case	Case 1	Case 2	Case 3
Mass particles (g)	175	175	175	175
Fluidized air flow (m^3/h)	40	40	40	40
Atomizer air flow (m^3/h)	3.0	3.0	3.0	3.0
Moisture content of inlet air (kg water/kg air)	0	0	0	5.1×10^{-3}
Temperature of inlet air (°C)	65	85	65	65
Initial air temperature (°C)	65	85	65	65
Coating mass flow from spray (g/min)	10	10	20	10
Initial dry content in the coating liquid (wt %)	20	20	20	20

Table 4. Dimensions of the Laboratory Scale Wurster bed

Geometric Dimension	Value
Diameter truncated cone, Under, Du (mm)	100
Diameter truncated cone, Upper, Do (mm)	250
Height of the truncated cone, Hc (mm)	320
Height of the expansion chamber, He (mm)	400
Height of the Wurster tube, Hw (mm)	60
Diameter of the Wurster tube, Dw (mm)	50
Gap between Wurster tube and distributor plate, Hg (mm)	15

fluidisation air and the particles in the Wurster bed are given in Tables 5 and 6. It is acknowledged that coating may change the particle properties, but this is not accounted for in the current study.

Numerical modeling

Wetting model

The moisture in the wetting model was assumed to be injected in a specified volume above the jet inlet, i.e., the wetting region. To estimate the liquid spray penetration depth into the bed, the particle volume fraction close to the spray inlet was calculated from the particle and gas flow under experimental conditions. The angle of the wetting region, which was determined from visual observations of the spray device, was found to be around 25°. The penetration depth of the droplets in the jet was estimated with Eqs. 19 and 20 and by using the results of the computations of the volume fraction of particles. Experiments in the laboratory scale Wurster bed under normal process conditions show a coating yield well above 95%. The yield depends both on drying of droplets before deposited on the particles and on attrition of the particles. In the model a 100% collection efficiency of droplets was assumed.

In the wetting region, a fixed value of water fraction in the particle phase was set. The water fraction in the wetting region was calculated from the experimentally determined

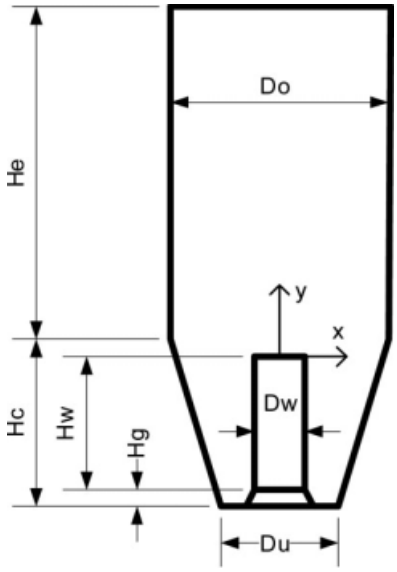

Figure 2. Dimensions of the laboratory scale Wurster bed.

Table 5. Particle Properties

Variable	Value
Diameter, d_p (m)	480×10^{-6}
Density, ρ_p (kg/m^3)	1500
Heat capacity, $c_{p,p}$ [J/(kg·K)]	840
Thermal conductivity, k [W/(m·K)]	0.41
Coefficient of restitution for particle collisions, e_{pp}	0.9
Kick-in volume fraction for frictional stress, $\alpha_{p,\,min}$	0.50
Maximum particle packing, $\alpha_{p,max}$	0.65
Angle of internal friction, Φ (°)	28
Constants in frictional pressure Eq. (31) Table 2	
Fr	$0.1\alpha_p$
nn	2
pp	3

spray rate of the coating solution and the average particle volume fraction passing the wet region. The average particle volume fraction in the wetting region was estimated from a 10 s simulation of the particle and gas flow.

The average particle volume fraction in a 1-cm high truncated cone with a 25° angle, above the jet inlet, was estimated to be 0.11. The wetting region was represented in the model by a space spanned by a 1-cm high truncated cone with a 25° angle; moisture content in the wetting region was calculated by dividing the liquid flow by the particle flow passing through. The particle flow passing the wetting region was determined by

$$\iint_{A2} \alpha_p |\mathbf{u}_p| dA \tag{19}$$

where $A2$ is the surface area at the top of the cone where the particles leave the wetting region, depicted in Figure 3 with a horizontal arrow. The average flow of particles is estimated, from 10 s of simulation time, as 1.2×10^{-5} m^3/s. Twenty-nine percentage of the particles passing the Wurster tube also pass the wetting region. A spray rate of 10 g/min gives a moisture content of 0.9 weight percent in the particle phase.

The height of the liquid layer was estimated by assuming that the coating liquid is spread equally over the surface of the particles passing the wetting region. The thickness of the liquid layer was calculated by first assuming a flat distribution of the liquid over the whole particle surface to 1.1 μm,

$$h_L = \frac{\dot{m}_L}{\rho_L} \Big/ \left(\frac{\dot{m}_p}{\rho_p} \frac{6}{d_p} \right) = 1.1 \times 10^{-6} m \tag{20}$$

A comparison was made of the estimated thickness of the liquid layer and the size of the droplet in the experimental set-up. The droplets from the spray nozzle have an average diameter of 10 μm. The equilibrium angle for a spread droplet of a typical coating liquid is assumed to be 30°. With these droplet properties, an average thickness of the droplet

Table 6. Air Properties

Variable	Value
Density, ρ_g (kg/m^3)	1.063
Heat capacity, $c_{p,g}$ [J/(kg K)]	1007
Thermal conductivity, k [W/(m K)]	0.0282
Viscosity, μ_g [kg/(m s)]	1.985×10^{-5}
Diffusivity of water in air, D_{AB} (m^2/s)	2.6×10^{-5}

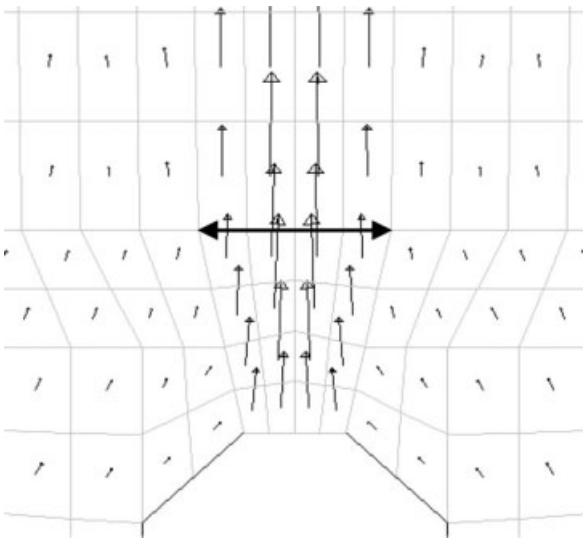

Figure 3. Particle velocity at the jet inlet.

is estimated to be 1.5 μm, which is higher than the thickness calculated with the assumption of a distribution of the liquid over the whole particle surface. Therefore, 73% of the particle surface is assumed to be wet, which corresponds to a 1.5-μm thick liquid layer; this agrees with the specified spray rate. More detailed studies of single particle coating are reported by Strom et al.[24] and Karlsson et al. (Submitted).

In case 2, the spraying rate is doubled (Table 3). Doubling the spray rate doubles the liquid height and, in analogy with the earlier discussion above, we assume that the entire particle surface is wetted with an equally thick film.

Initial conditions

The particle phase, with a particle volume fraction of 0.3 was initially placed in the bottom of the equipment. The initial particle velocity was set to zero, and the initial gas velocity was set to 0.1 m/s in the vertical direction. After 0.5 s simulation, the particle and gas dynamics have a circulating motion in the bed, and the average distribution of the phases in the domain has reached a stationary state. When this averaged stationary state was obtained, the equations describing the wetting and drying were added to the simulation. The initial temperature was set to the gas temperature at the inlet for both the particle and gas phases. The initial moisture content of both the particle and gas phases was set to zero.

Boundary conditions

In the experimental set-up, the fluid flow passes through a plate with small holes, the distributor plate, before entering

Table 7. Gas Inlet Velocity

Zone on the Distributor Plate: Radial Distance From the Jet Center (mm)	Inlet Velocity (m/s)
0–2.5 (jet)	44.20
11–27	1.26
27–45	0.23
45–50	2.38

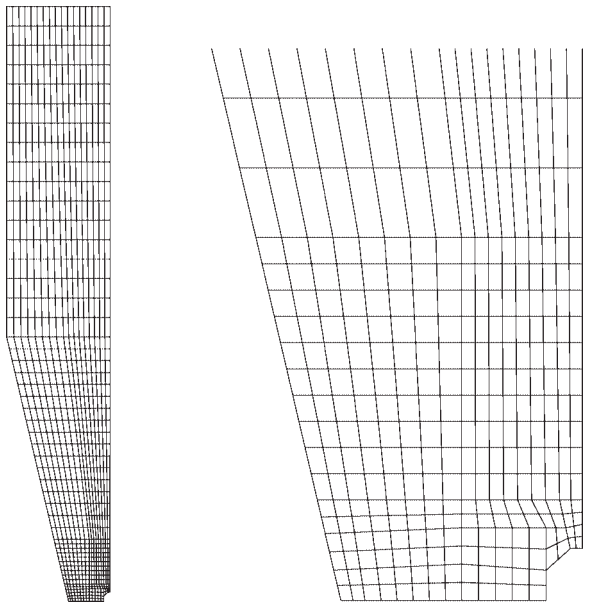

Figure 4. The computational grid of the Wurster equipment with 842 cells.

The vertical boundaries are walls (left) and axi-symmetric rotational axis (right).

the bed. The size of the openings in the distributor plate varies over the plate to get a favorable distribution of the air into the bed. The distributor plate is divided into three circular regions with differently distributed holes. The first region is around the jet under the Wurster tube, the second is under the annulus, and the third is at the edge of the plate. The boundary conditions for the gas velocity were set to match the gas flow speed from the holes. Equations for the pressure drop, due to change of the cross-section area when the air passes the distributor plate, were used to estimate the distribution of the air flow over the plate. To avoid dead zones of particles at the edge of the plate, the part with holes, and thus the velocity, is highest close to the wall. The velocity is higher in the region under the Wurster tube than outside, to promote the transport of particles up through the tube. The four velocities are specified as velocity inlet conditions in the simulation, Table 7.

The jet area used in the simulations is slightly larger than in the experimental set-up because the physical jet diameter

Table 8. Variables in Experiment and in the Simulation

Variable	Value
Particle diameter (μm)	550
Particle density (kg/m^3)	1370
Particle heat capacity, c_p (J/kg, K)	840
Mass particles (g)	200
Fluidised air flow (m^3/h)	40
Atomizer air flow (m^3/h)	2.7
Moisture content in air at inlet (kg water/kg air)	0
Temperature air at inlet (°C)	35
Initial temperature (°C)	35
Coating flow experiments (g/min)	3.0–9.7
Coating flow simulation (g/min)	3.7
Heat loss (W/m^2)	114.5
Initial dry content in the coating liquid (wt %)	26

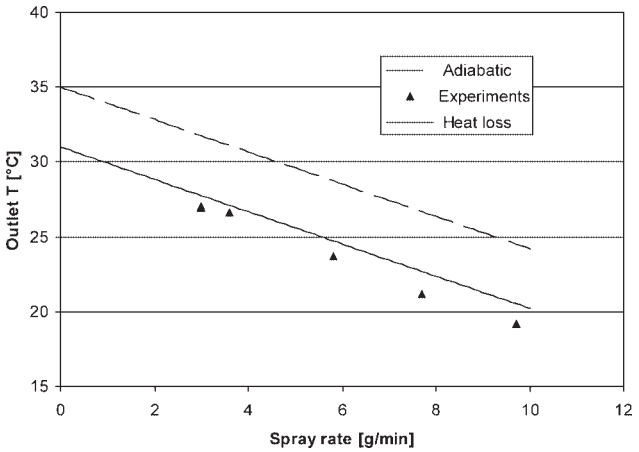

Figure 5. Bed outlet air temperature versus spray rate.

could not be resolved, due to grid restrictions. Because the gas mass flow rate in the simulations is the same as that used in the experiments, a momentum source is required to compensate for the larger jet area. Calculations of the magnitude of this source term, however, show that the effect of the additional momentum source term is negligible. The boundary conditions at the walls were no slip for the gas and free slip for the particle phase. Atmospheric pressure was assumed at the outlet of the bed.

Simulations

In this study, the commercial code Fluent 6.3.26 from ANSYS was used. A two-dimensional mesh with ~800 cells was chosen in the simulation. As the equipment has cylindrical symmetry, an axi-symmetric boundary condition was used in the centre of the bed, Figure 4, to enable faster calculation.

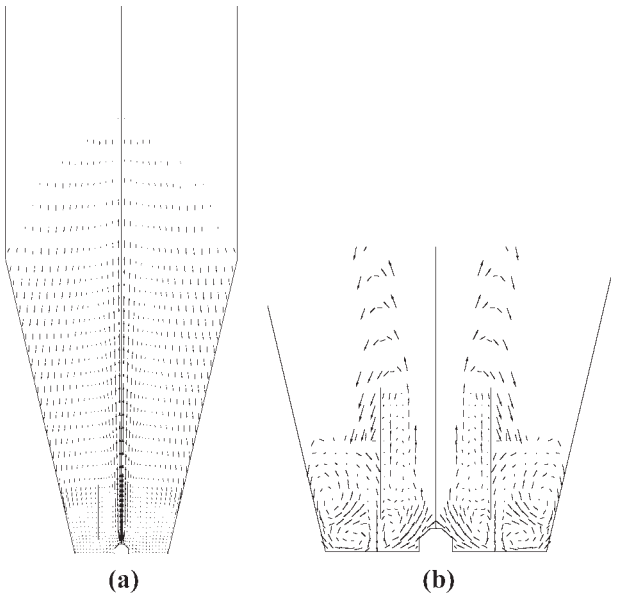

Figure 6. A "snapshot" of the particle velocity after 50 s simulation.

(a) The particle velocity in the whole bed, and (b) the velocity vectors smaller than 0.5 m/s.

A second-order-upwind discretization scheme was used for the discretization of all advective terms. The phase coupled SIMPLE algorithm was used for the pressure velocity coupling. Refinement of the mesh up to 4500 cells was used to study grid independency of the averaged stationary-state results. Both the fine and the coarse grids showed similar particle and gas flow patterns. The unsteady simulations were run in time, until an average stationary state of the particle moisture content and temperature in the bed were obtained.

Results and Discussion

Experimental validation

Particle and Gas Motion. The multiphase CFD model of the particle and gas dynamics was compared with data from the study of Karlsson et al.[25] A simulation of the bed used by Karlsson et al.[25] was made to evaluate the particle and gas model. The particle movement in the fountain region was measured with a high speed video camera. A laboratory scale Wurster bed made of Plexiglas was used to get optical

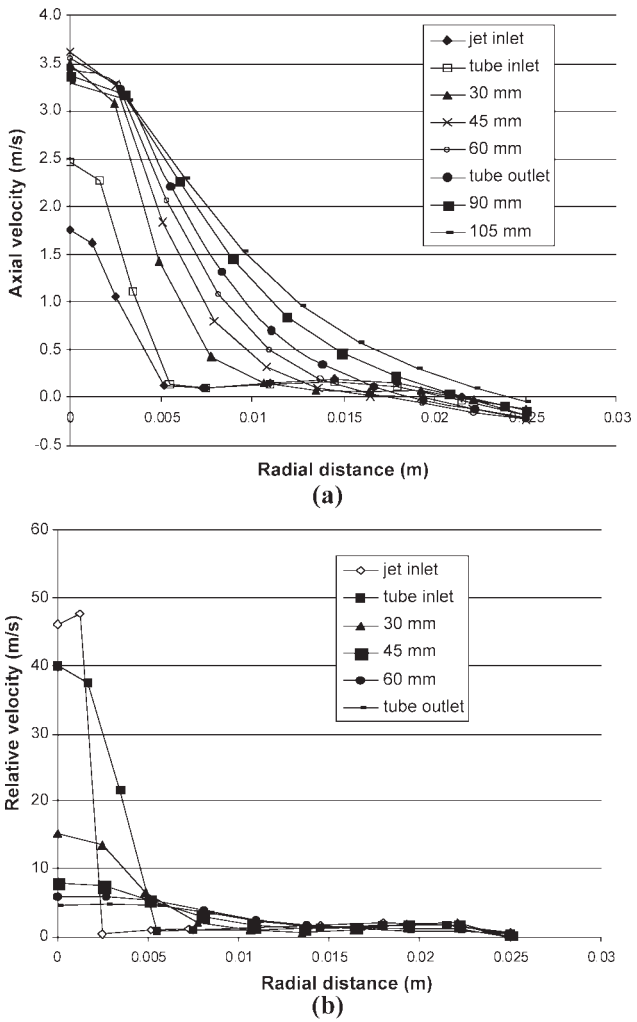

Figure 7. Mean velocities versus radial distance from the bed center at selected heights.

(a) Particle axial velocity and (b) relative velocity between the particle and gas phases.

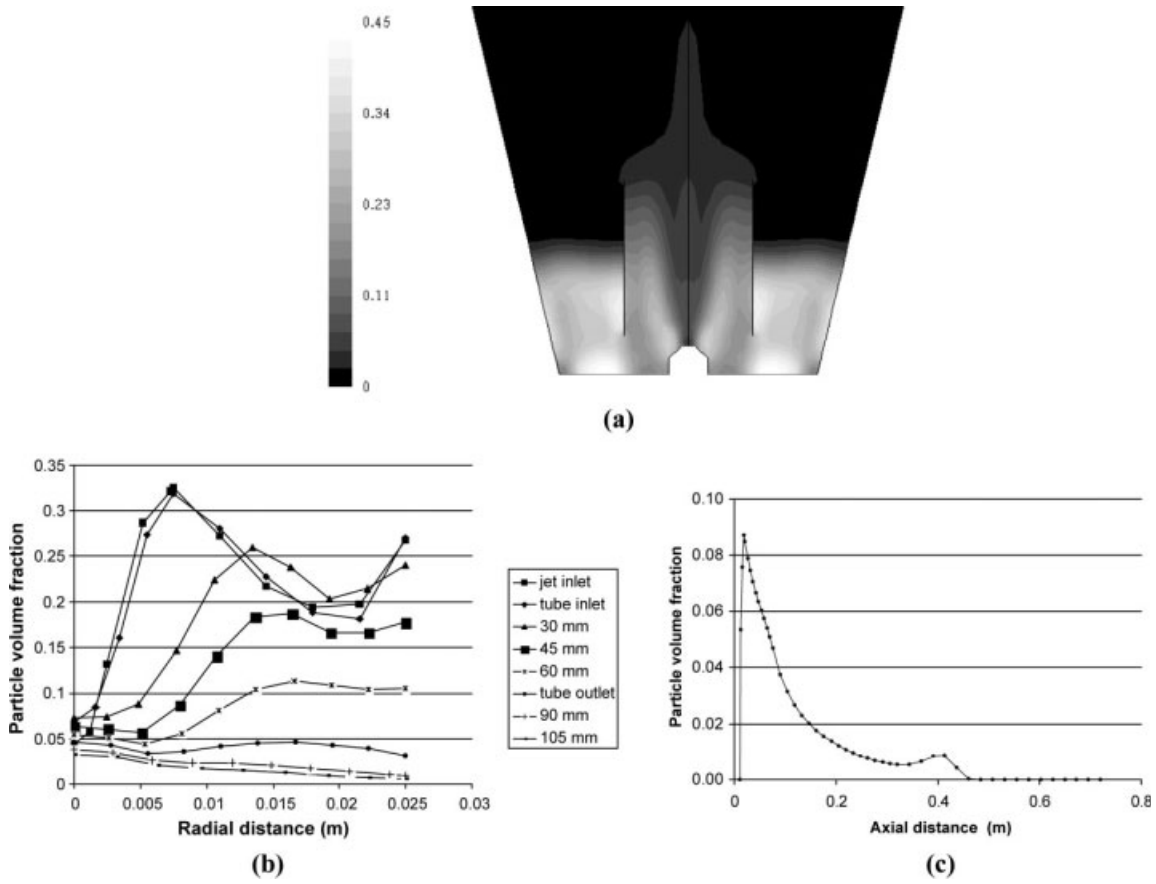

Figure 8. Mean particle volume fraction during 50 s.

(a) Particle volume fraction, (b) variation of particle volume fraction at selected heights, and (c) variation of the particle volume fraction along the center axis.

access to the flow. The Plexiglas bed, which is smaller than the laboratory scale bed, was chosen to get optical access through the bed to the fountain region. The geometric dimensionless relations between the top and bottom diameters of the truncated cone, the bottom diameter and the height of the truncated cone, as well as the bottom diameter of the truncated cone and the diameter of the Wurster tube, are all equal for the Plexiglas bed[25] and the laboratory scale bed simulated in this study. Hydrodynamic similarity, on the other hand, is not ensured.

The height of the fountain in the simulation and the experiments is of the same order of magnitude; an increase

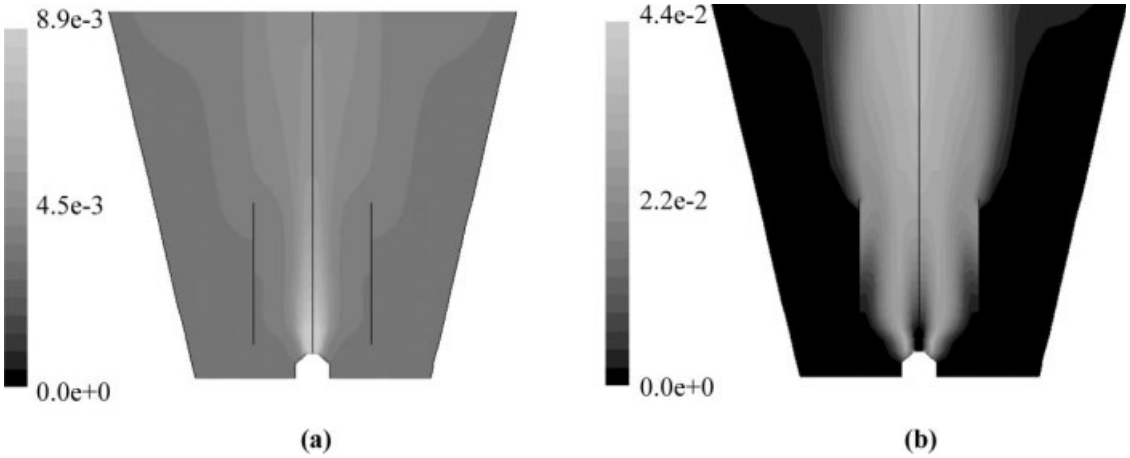

Figure 9. Moisture content.

(a) Particle phase and (b) gas phase after 50 s simulation of the base case.

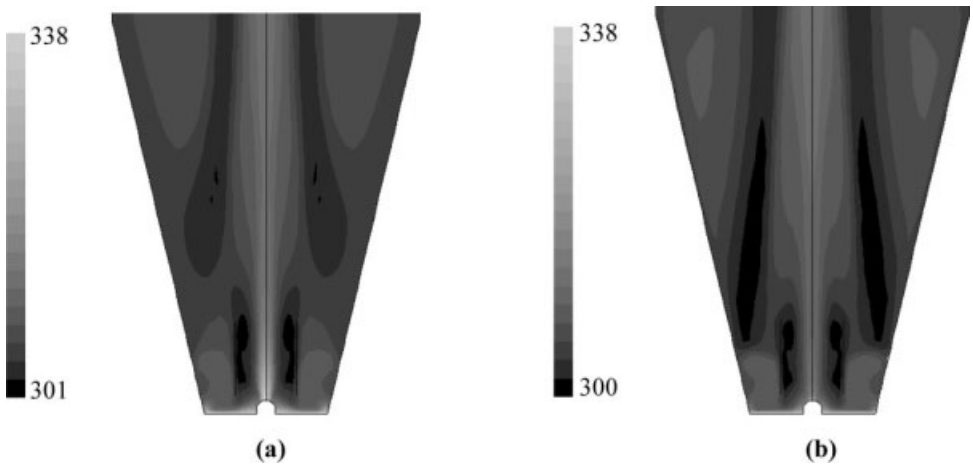

Figure 10. Temperature in K after 50 s simulation of the base case.

(a) Gas and (b) particle.

in jet velocity causes an increase in fountain height, which agrees with the experimental results. The influences of the amount of particles and the Wurster tube gap diverge from the experimental results. From the experiments, it was observed that a reduction of the amount of particles reduces the fountain height, and a decrease of tube gap increases the fountain height. The simulation of a decreased Wurster tube gap produced approximately the same fountain height as in the base case, while the simulation of a smaller amount of particles produced a higher fountain.

The jet is modeled as a velocity inlet with a velocity direction normal to the distributor plate. The influence of the distribution of the air between the annulus and the Wurster tube is central to the fountain height; the simplified boundary conditions can be an explanation for the differences between the experiments and the simulations. In the present study, the simplified model is used in order to obtain fast simulations of the fluid dynamics.

Heat and Mass Transfer. The temperatures and moisture contents in the air, at the bed inlet and outlet were measured during the coating. A temperature profile 2 cm in from the chamber wall was also measured. In the simulations, the particle and operating parameters were as close as possible to the values from the experiment, Table 8. The numerical simulation shows the correct characteristic circulation motion for the particles in the bed. The mean particle flow through the spray region was calculated from a simulation of the particle and gas dynamics; the moisture content for a particle passing the wetting region was estimated to be 0.41 weight percent for a spray rate of 3.7 g/min.

In Figure 5 experimental outlet air temperatures are compared with estimated temperatures with heat losses and under adiabatic conditions respectively. The temperature decreases due to evaporation of moisture, and the thermal energy sink is estimated assuming that the coating will dry to 64% dry content. The experimental values for air temperature at the outlet of the bed are represented by triangles in the figure. Experimental values for the temperature are around 5°C lower than the values obtained in the simulations. The lower temperature in the experiments can be explained by heat loss through the equipment walls. The heat loss was estimated by running the equipment without the liquid. This produced a 4°C lowering of the air temperature passing the bed. From this experiment, a heat flux from the walls was estimated as 114.5 W/m^2. The heat flux was specified as a boundary condition at the outer walls in the simulation. The temperatures at the outlet and along the wall, in the model with heat flux from the outer walls, are of the same order of magnitude as in the experiment. The magnitude of the simulated moisture content in the air at the bed outlet also agrees with the

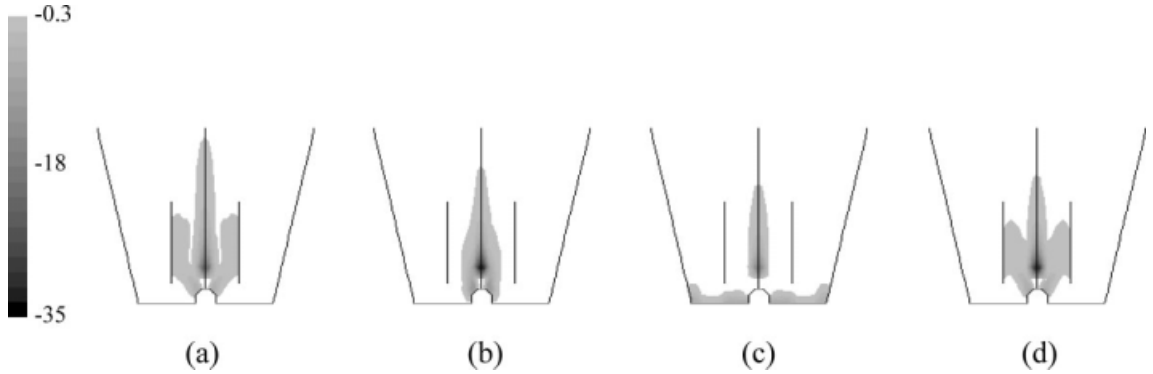

Figure 11. Mass transfer between the phases in (kg/s, m^3).

(a) Base Case, (b) Case 1, (c) Case 2, and (d) Case 3.

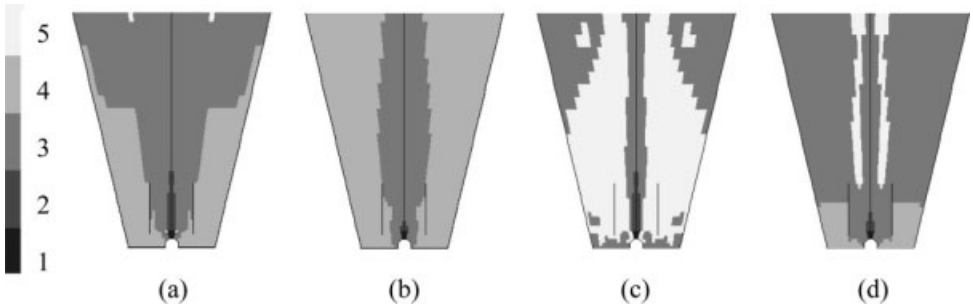

Figure 12. Drying region scale.

1, Wetting region; 2, $dc \leq dc_c = 0.40$; 3, $0.40 < dc \leq 0.64$; 4, $dc > dc_e = 0.64$; 5, Saturated air; (a) base case, (b) case 1, (c) case 2, and (d) case 3.

experiments. The experimentally obtained value was 0.0040 kg moisture/kg dry air. In the simulations the value slowly varies in "time" between 0.0032 and 0.0042 kg moisture/kg dry air, because the amount of particles passing the spray region varies slightly.

Numerical simulation of the particle and gas motion

The numerical simulation results show the characteristic circulation motion of the particles in the laboratory scale Wurster process. A "snapshot" of the simulation results for the particle velocity field after 50 s is shown in Figure 6. The jet accelerates the particles through the Wurster tube; the particle velocity is highest in the middle of the jet, about 5 cm above the jet inlet, see Figure 7a. The relative velocity between the particle and gas phases influences the mass transfer rate. Relative velocity as a function of the radial distance at selected heights in the tube is shown in Figure 7b. When the particles enter the expansion region, the gas velocity, and thus the particle velocity, decreases due to an increase in area. The particles fall down towards the wall and enter the dense region of particles where the particle velocity is relatively low.

In Figure 6b the maximum particle velocity is shown as a vector plot, where only the vectors with a velocity less than 0.5 m/s are shown, to be able to visualize the low particle velocity in the dense region. The high inlet velocity close to the chamber wall gives the particles an upward motion. The low inlet velocity, in the region outside the Wurster tube, gives a high volume fraction of particles close to the distributor plate, Figure 8a. High particle volume fraction was also observed at the inclined surface around the nozzle. This inclined surface is treated as a wall in the simulation; thus, the particles can accumulate here. From the dense region at the sides, the particles are transported into the jet again. Particles in the middle of the jet are transported through the tube, but the particles further from the centre of the jet fall down through the tube close to the tube wall, which can be seen from Figure 6b. The particle circulation time is estimated to be about 5.4 s by dividing the total amount of particle by the flow of particles through the Wurster tube.

Figure 8 shows the mean distribution of the particles in the bed during 50 s. The height of the bed in the annulus is approximately 0.05 m. The particle volume fraction, versus radial distance from the bed centre at selected heights, is shown in Figure 8b; it is lowest in the centre of the tube. The particle volume fraction in the centre of the bed versus height is plotted in Figure 8c; the plot shows a fountain height of 0.45 m.

Drying in the bed

The simulations were continued until a stationary state value of the average moisture and the temperature were achieved in the bed. After ~40 s simulation, the average moisture content and the temperature in the bed stop rising. The moisture content varies around an average value in relation to the variation of particle flow through the wetting region. The moisture content of the particle phase and the gas phase are shown in Figure 9. The moisture content in the particle phase starts at 0.9 wt %, specified in the wetting region, and decreases when the particles pass through the tube. Figure 11a shows the mass transfer for the base case in a snapshot taken after 50 s of simulated time. After leaving the wetting region, the particle drying is described by Eq. 10. The mass transfer decreases with height in the Wurster tube, which is caused by both the increasing amount of

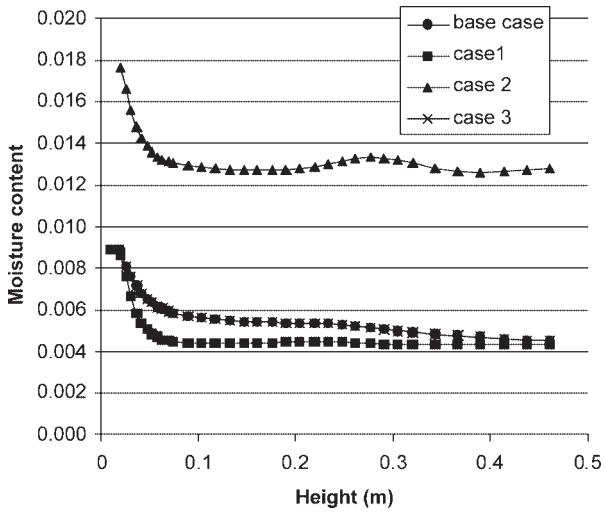

Figure 13. Moisture content in the particle phase at the centre of the bed.

moisture in the gas phase and the decreasing relative velocity between the phases. After the moisture content has fallen to a critical value, the drying rate starts to decrease according to Eq. 12. The liquid layer reaches a dry content of 64 volume percent as the particles are falling, and the mass transfer is stopped. In the base case, most of the mass transfer takes place in the Wurster tube. Evaporation of the water to the gas phase reduces the temperature in both the particle and gas phases, Figure 10.

The base case was used as a numerical starting point for the other cases, and the iteration was run until the moisture and temperature reached an average stationary state value again. The mass transfer between the phases, $S_{w,p}$ in Eq. 9, and the drying regions for the four cases are summarized in Figures 11 and 12, respectively. The gray scale in Figure 11 is from -35 (kg/s, m^3) to -0.3 (kg/s, m^3); the minus sign shows that the water is transferred from the particles to the gas.

From Figures 11–13, it can be seen that the maximum mass transfer rate is higher for the higher temperature, Case 1, and the particles dry faster, as is expected. The higher temperature gives a higher concentration of water at the particle interface, which increases the driving force for mass transfer. With the high temperature, there are no regions with saturated air, Figure 12b. The higher temperature of the air raises its capacity for moisture content before the air is saturated; hence there are no regions with saturated air.

In case 2, the spray rate is increased from 10 to 20 g/min. In this case the particles do not reach the limit of 64% of latex particles in the liquid layer. The air becomes saturated with water and the drying stops. The particles have higher moisture content even in the dense region, and the drying process continues near the distributor plate where dry air enters the bed. The temperature is around 6°C lower than in the base case; this lower temperature is explained by the higher energy requirement for drying the particles.

In case 3, the moisture content of the air entering the bed is set to 5.1 g water/kg dry air, which is equivalent to 35% RH at 20°C. The drying in the centre of the bed agrees with the base case, Figure 13. However, larger regions with saturated air will occur with the higher moisture content in the air entering the bed; the level will reach a limit of 64% of latex particles in the coating layer later, Figure 12d.

Conclusions

A detailed model of the Wurster process with a continuous injection of liquid was developed and validated with experimental work. The particles are modeled as an Eulerian phase and their rheology is described with the kinetic theory of granular flow. The continuous injection of liquid through a spray nozzle is modeled by specifying the moisture content for the particle phase when passing a region close to the liquid inlet. The particle moisture content at the liquid inlet is estimated by experimental conditions and by determining the volume fraction and particle flow rate close to the inlet. The model, which shows the characteristic cycle motion of the particles in the bed, is in good agreement with our experimental observations. The simulated fountain height of the particles agrees well with measurements of the particle trajectories in the fountain. Moreover, the simulation of the air temperature shows good agreement with experimental air temperatures at the outlet of the bed.

The influence of the drying region and mass transfer between the phases for different spray rates, temperature, and moisture content was shown. The higher spray rate produced more water to evaporate and, hence, lower temperature and more regions with saturated air. Higher temperature gave faster drying of the particles, and no regions with saturated air were revealed by the simulation. The higher moisture content at the air inlet normal for the production scale produces more saturated air.

Notation

C_D = drag coefficient
d = diameter, m
dc = dry volume content in the coating layer
dz = average droplet path length, m
D_{AB} = diffusion coefficient, m^2/s
e_{pp} = coefficient of restitution for particle collisions
g = gravity vector, m/s^2
g_0 = radial distribution function
h_L = liquid height, m
h_{pg} = heat transfer coefficient, W/m^2, K
H_i = Enthalpy of phase i, J/kg
$H_{vap,w}$ = latent heat of water, J/kg
I_{2D} = second invariant of the strain rate tensor, s^{-2}
J_p = exchange of fluctuating energy between phases, kg/m, s^3
k_{pg} = mass transfer coefficient, m/s
m_1 = spray rate, kg/s
m_p = particle mass flow, kg/s
M = molecular weight, kg/mol
$N_{w,p}$ = mass flux, kg/m^2, s
Nu = Nusselt number
p = pressure, N/m^2
Pr = Prandtl number
$Q_{j,i}$ = heat transfer between the particle and gas phases, W/m^3
R = molar gas constant, J/mol, K
Re = Reynolds number
s = droplet deposition, kg/s, m^3
$S_{h,i}$ = energy transfer between the particle and gas phases due to evaporation, W/m^3
$S_{w,i}$ = mass transfer between the particle and gas phases, kg/m^3, s
Sc = Schmidt number
Sh_p = Sherwood number
t = time, s
T = temperature, K
u = velocity vector, m/s
u'_p = fluctuating particle velocity vector, m/s
w = mass fraction of water, (kg water/kg dry particles)

Greek letters

α = volume fraction
β = interface momentum transfer coefficient, kg/m^3, s
γ_p = dissipation of granular energy due to collision, kg/m, s^3
Γ = diffusion coefficient of scalar variable, kg/m, s
κ_p = diffusion coefficient of granular energy, kg/m, s
λ = bulk viscosity, Pa s
μ = shear viscosity, Pa s
ρ = density, kg/m^3
$\bar{\tau}$ = viscous stress tensor, N/m^2
ϕ = angle of internal friction, °
ϕ_{gp} = energy exchange between the gas and the particle phases
Θ_p = granular temperature, m^2/s^2

Subscripts

g = gas phase
i = gas phase or particle phase
j = gas phase or particle phase

L = liquid
max = maximum
min = minimum
n = nozzle
p = particle phase
sat = saturated
w = water

Literature Cited

1. Maronga SJ, Wnukowski P. Establishing temperature and humidity profiles in fluidized bed particulate coating. *Powder Technol.* 1997;94:181–185.
2. Vanderhoff J, Bradford E, Carrington W. The transport of water through latex films. *J Polym Sci Symp.* 1972;41:155–174.
3. Christensen FN, Bertelsen P. Qualitative description of the Wurster-based fluid-bed coating process. *Drug Dev Ind Pharm.* 1997;23:451–463.
4. Sherony DF. A model of surface renewal with application to fluid bed coating of particles. *Chem Eng Sci.* 1981;36:845–848.
5. Maronga SJ, Wnukowski P. Modelling of the three-domain fluidized-bed particulate coating process. *Chem Eng Sci.* 1997;52:2915–2925.
6. Turton R. Challenges in the modeling and prediction of coating of pharmaceutical dosage forms. *Powder Technol.* 2008;181:186–194.
7. Magnusson A, Rundqvist R, Almstedt AE, Johnsson F. Dual fibre optical probe measurements of solids volume fraction in a circulating fluidized bed. *Powder Technol.* 2005;151:19–26.
8. Szafran RG, Kmiec A. CFD modeling of heat and mass transfer in a spouted bed dryer. *Ind Eng Chem Res.* 2004;43:1113–1124.
9. Ishii M. *Thermo-Fluid Dynamic Theory of Two-Phase Flow*. Paris: Eyrolles, 1975.
10. van Wachem BGM, Schouten JC, van den Bleek CM, Krishna R, Sinclair JL. Comparative analysis of CFD models of dense gas-solid systems. *AIChE J.* 2001;47:1035–1051.
11. Ding J, Gidaspow D. Bubbling fluidization model using kinetic theory of granular flow. *AIChE J.* 1990;36:523–538.
12. Jenkins JT, Savage SB. Theory for the rapid flow of identical, smooth, nearly elastic, spherical particles. *J Fluid Mech.* 1983;130: 187–202.
13. Lun CKK, Savage SB, Jeffrey DJ, Chepurniy N. Kinetic theories for granular flow: inelastic particles in couette flow and slightly inelastic particles in a general flow field. *J Fluid Mech.* 1984;140:223–256.
14. Gidaspow D, Bezburuah R, Ding J. *Hydrodynamics of circulating fluidized beds: kinetic theory approach. Fluidization, VII: Proceedings of the 7th Engineering Foundation Conference on Fluidization.* Engineering Foundation, New York: 1992: 75–82.
15. Zhang DZ, Rauenzahn RM. A viscoelastic model for dense granular flows. *J Rheol.* 1997;41:1275–1298.
16. Johnson PC, Jackson R. Frictional collisional constitutive relations for antigranulocytes-materials, with application to plane shearing. *J Fluid Mech.* 1987;176:67–93.
17. Schaeffer DG. Instability in the evolution equations describing incompressible granular flow. *J Differ Equations.* 1987;66:19–50.
18. Wen CY, Yu YH. Mechanics of fluidization. *Chem Eng Progr Symp Ser.* 1966;62:100–111.
19. Löffler F, Dietrich H, Flatt W. *Dust Collection with Bag Filters and Envelope Filters*. Braunschweig/Wiesbaden: Friedr Vieweg & Sohn, 1988.
20. Heinrich S, Blumschein J, Henneberg M, Ihlow M, Peglow M, Morl L. Study of dynamic multi-dimensional temperature and concentration distributions in liquid-sprayed fluidized beds. *Chem Eng Sci.* 2003;58:5135–5160.
21. Hidayat M, Rasmuson A. Heat and mass transfer in U-bend of a pneumatic conveying dryer. *Chem Eng Res Des.* 2007;85:307–319.
22. Erkselius S. *Film Formation from Dispersions, Preparation and Mechanisms*. Lund, Sweden: PhD Thesis, Department of Polymer Science and Engineering, Lund University, 2006.
23. Gunn DJ. Transfer of heat and mass to particles in fixed and fluidized beds. *Int J Heat Mass Transfer.* 1978;21:467–476.
24. Strom D, Karlsson S, Folestad S, Niklasson Bjorn I, Laurell T, Nilsson J, Rasmuson A. A new device for coating single particles under controlled conditions. *Chem Eng Sci.* 2005;60: 4647–4653.
25. Karlsson S, Niklasson Bjorn I, Folestad S, Rasmuson A. Measurement of the particle movement in the fountain region of a Wurster type bed. *Powder Technol.* 2006;165:22–29.

Manuscript received Dec. 21, 2007, revision received Oct. 28, 2008, and final revision received Jun. 22, 2009.